

Recent Progress in Electrical Impedance Tomography

Martin Hanke and Martin Brühl

Fachbereich Mathematik und Informatik, Johannes Gutenberg-Universität,
55099 Mainz, Germany

E-mail: hanke@math.uni-mainz.de, bruehl@math.uni-mainz.de

Abstract. We consider the inverse problem of finding cavities within some body from electrostatic measurements on the boundary. By a cavity we understand any object with a different electrical conductivity than the background material of the body. We survey two algorithms for solving this inverse problem, namely the factorization method and a MUSIC-type algorithm. In particular, we present a number of numerical results to highlight the potential and the limitations of these two methods.

Submitted to: *Inverse Problems*

AMS classification scheme numbers: 65N21, 35J25, 35R30

1. Introduction

Electrical impedance tomography is a technique to recover spatial properties of the interior of a conducting object from electrostatic measurements taken on its boundary. For example, a current through a homogeneous object will in general induce a different electrostatic potential than the same current through a similar object with an enclosed cavity. In fact, the latter one will depend on the size, the precise location, and the electrical properties of the cavity. In other words, it should be possible to use boundary measurements of the potential to detect and locate such cavities, an important task in nondestructive testing.

A related, but more ambitious problem is the following. Consider an object with a spatially varying smooth electric conductivity. Is it possible to reconstruct this conductivity, just by means of measuring the boundary potentials for a set of current patterns imposed on the boundary of the object? The answer for this question turns out to be extremely difficult, but is now known to be positive (Nachman [28, 29]): If the boundary potentials are known for all current patterns (from a reasonable function space), then there is no second smooth conductivity distribution which fits these data.

The same result is true for the aforementioned problem of finding one or a finite number of cavities within an object, cf. Kohn and Vogelius [25], and Isakov [21], but it is tempting to believe that less data are necessary for its solution. Up to now, however, only partial results of this sort are known, cf., e.g. [2, 16, 32].

When it comes to the design of numerical algorithms for solving either of the two problems, other difficulties show up. Loosely speaking, electrical currents with high spatial frequency prefer to travel close to the surface of the object, from one source on the boundary to a neighboring sink. Very little current really traverses the object. As a consequence, differences in the conductivity near the center of the object have hardly any effect on the electrical field and the boundary potentials which are measured. Or, from an inverse problem point of view, small measurement errors are easily mistaken to be caused by disturbances in the conductivity distribution in the interior of the body.

In mathematical terms this means that electrical impedance tomography is an ill-posed problem. In fact, it is severely ill-posed by all known measuring scales, cf. [1, 27, 15]. As such, it is important to incorporate as much a priori knowledge about the object as possible, and this is the reason why the cavity problem may be somewhat easier to approach, and more likely to eventually solve numerically.

In this paper we focus on our own contributions to this particular aspect of impedance tomography; for a somewhat broader point of view we refer to the recent surveys by Cheney, Isaacson, and Newell [10], and by Borcea [3]. We will discuss the most interesting details of two algorithms that we have developed, and present numerical results for a variety of different setups. Some of these results have been published before, cf. [4, 6, 7, 8], but we also include new results, most of which are concerned with the issue of restricted data.

The exposition of the paper is as follows. In Section 2 we introduce our notations and review well-known facts about the direct problem, in particular we define the fundamental Neumann-Dirichlet operator. Subsequently, in Section 3, we briefly sketch the theoretical foundation of our first method for solving the inverse problem. Because it is based on a factorization of the difference of two Neumann-Dirichlet operators we call it the *factorization method*. The key steps of its numerical implementation are described in Section 4. There we also include a first reconstruction obtained by Schappel [31] for the half plane geometry. In Section 5 we turn to the question of regularization which is indispensable for any kind of ill-posed problem, and discuss the limitations of the factorization method in the presence of noise. The second method is the so-called *MUSIC algorithm*, which is the topic of Section 6. It has interesting similarities to the factorization method and is particularly useful for noisy data. From Section 7 onwards we focus on extensions of our methods to various kinds of restricted data. We present numerical results for the so-called limited angle problem in Section 7, and for finite electrode systems in Section 8. In this final section we also present our first reconstructions from real data sets which were kindly provided by Jon Newell and his colleagues at the Rensselaer Polytechnic Institute. The paper concludes with a few remarks and an appendix which contains a new and interesting side aspect for our approach.

2. Neumann-Dirichlet operators

We consider an object covering a bounded domain B in \mathbb{R}^n , $n = 2$ or 3 , with boundary $T = \partial B$. It will be assumed that the object is homogeneous and conducting except for a number of insulating cavities Ω_j , $j = 1, \dots, p$ (the latter assumption can be relaxed substantially). These are domains whose closures are mutually disjoint and contained in B . We denote by Ω the union of the cavities and by $\Gamma = \partial\Omega$ the boundary of Ω . T and Γ are considered to be sufficiently smooth, with ν being the outer (relative to

$B \setminus \overline{\Omega}$) unit normal vector.

It is well-known that for a prescribed boundary current

$$f \in \mathcal{L}_\diamond^2(T) = \{f \in \mathcal{L}^2(T) : \int_T f(s) ds = 0\}$$

the electrostatic potential u in the object satisfies the Laplace equation

$$\Delta u = 0 \quad \text{in } B \setminus \overline{\Omega} \quad (2.1)$$

with boundary conditions

$$\frac{\partial u}{\partial \nu} = f \quad \text{on } T, \quad \frac{\partial u}{\partial \nu} = 0 \quad \text{on } \Gamma. \quad (2.2)$$

This Neumann problem (2.1), (2.2) has a unique solution

$$u \in H_\diamond^1(B \setminus \overline{\Omega}) = \{u \in H^1(B \setminus \overline{\Omega}) : \int_T u(s) ds = 0\},$$

and the corresponding boundary potential $g = u|_T$ again belongs to $\mathcal{L}_\diamond^2(T)$ by the standard trace theorem.

It is this function $g \in \mathcal{L}_\diamond^2(T)$ which can be measured without physical damage of the object, and which we will compare in the sequel with the boundary potential $g_0 \in \mathcal{L}_\diamond^2(T)$ for the same input current f and an object *without* cavities. That is, $g_0 = u_0|_T$, where $u_0 \in H_\diamond^1(B)$ solves the boundary value problem

$$\Delta u_0 = 0 \quad \text{in } B, \quad \frac{\partial u_0}{\partial \nu} = f \quad \text{on } T. \quad (2.3)$$

This defines two mappings

$$\Lambda : \begin{cases} \mathcal{L}_\diamond^2(T) & \rightarrow \mathcal{L}_\diamond^2(T), \\ f & \mapsto g, \end{cases} \quad \text{and} \quad \Lambda_0 : \begin{cases} \mathcal{L}_\diamond^2(T) & \rightarrow \mathcal{L}_\diamond^2(T), \\ f & \mapsto g_0, \end{cases}$$

called the Neumann-Dirichlet operators associated with the two boundary value problems (2.1), (2.2), and (2.3), respectively. While these two operators are linear, the function which maps Ω to Λ is necessarily nonlinear: The latter function, however, is the one we need to invert in our electrical impedance tomography problem.

The difference in the boundary potentials, $h = g - g_0$, is a function from the range of the operator $\Lambda - \Lambda_0$, i.e.,

$$h = (\Lambda - \Lambda_0) f. \quad (2.4)$$

Like any other function out of this range, h is the trace of a harmonic potential $w = u - u_0$ on $B \setminus \overline{\Omega}$. Moreover, by (2.2) and (2.3), the flux $\partial w / \partial \nu$ vanishes everywhere on T . Therefore, this potential w is uniquely determined as the solution of the Cauchy problem

$$\Delta w = 0, \quad w = h \quad \text{on } T, \quad \frac{\partial w}{\partial \nu} = 0 \quad \text{on } T, \quad (2.5)$$

cf., e.g., Dautray and Lions [13, Ch. II, §2, Corollary 11]. For the moment we refrain to specify the domain of harmonicity of w in (2.5). All we require is that w is harmonic in a neighborhood of T . In the particular case that h belongs to the range of $\Lambda - \Lambda_0$ the solution w of (2.5) is harmonic in $B \setminus \overline{\Omega}$, and may even have a harmonic extension beyond the boundary of the cavities.

Still, the above observation could emerge into a preliminary algorithm for the reconstruction of the cavities. To this end we introduce the dipole

$$D_z(x) = \frac{1}{\omega_n} \frac{(z-x) \cdot d}{|z-x|^n}, \quad x \neq z, \quad (2.6)$$

located in z with axis \ddagger $d \in \mathbb{S}^n$, $|d| = 1$, and augment it by a harmonic function v_z in B with Neumann data

$$\frac{\partial v_z}{\partial \nu} = -\frac{\partial D_z}{\partial \nu} \quad \text{on } T. \quad (2.7)$$

Here, ω_n is the surface measure of the unit sphere in \mathbb{R}^n . Then

$$H_z = D_z + v_z \quad (2.8)$$

is harmonic in $B \setminus \{z\}$ with vanishing flux $\partial H_z / \partial \nu$ on T . Therefore, if the trace

$$h_z = H_z|_T \quad (2.9)$$

of H_z belongs to the range of $\Lambda - \Lambda_0$, then z must be a point within the cavity Ω . (This follows from the uniqueness of the solution of the Cauchy problem (2.5), for then H_z has a harmonic extension onto $B \setminus \overline{\Omega}$, and thus its singularity at $x = z$ must lie in Ω .) Unfortunately, the converse is not true: h_z may fail to belong to the range of $\Lambda - \Lambda_0$, although $z \in \Omega$ and thus H_z is harmonic in $B \setminus \overline{\Omega}$ (see also the Appendix). This means that the range of $\Lambda - \Lambda_0$ is somewhat too small for the converse statement, but still we could use such a sort of test, i.e., whether h_z is in the range of $\Lambda - \Lambda_0$ or not, to find at least a subset of Ω . In the next section, however, we will see that we can do much better.

3. The square root of $\Lambda - \Lambda_0$

In this section we briefly sketch the theoretical background of the factorization method. We first survey the basic properties of the Neumann-Dirichlet operators Λ and Λ_0 , and introduce positive powers of $\Lambda - \Lambda_0$. Subsequently we characterize the range of the square root of $\Lambda - \Lambda_0$.

3.1. Positive powers of $\Lambda - \Lambda_0$

Given a boundary current f , the Thompson principle states that u_0 minimizes

$$J_0(v) = \frac{1}{2} \int_B |\text{grad } v|^2 dx - \int_T f v ds$$

among all $v \in H_\diamond^1(B)$, whereas u minimizes

$$J(v) = \frac{1}{2} \int_{B \setminus \overline{\Omega}} |\text{grad } v|^2 dx - \int_T f v ds$$

among all $v \in H_\diamond^1(B \setminus \overline{\Omega})$. The minima are given by

$$J_0(u_0) = -\frac{1}{2} \int_T f u_0 ds \quad \text{and} \quad J(u) = -\frac{1}{2} \int_T f u ds. \quad (3.1)$$

The respective Euler equations yield the weak forms of the two problems, like

$$\int_B \text{grad } u_0 \cdot \text{grad } v dx = \int_T f v ds \quad \text{for all } v \in H_\diamond^1(B)$$

for problem (2.3). Therefore, if v is the solution of problem (2.3) for a second input current $g \in \mathcal{L}_\diamond^2(T)$, then $\Lambda_0 g = v|_T$ and

$$\langle f, \Lambda_0 g \rangle_{\mathcal{L}^2(T)} = \int_T f v ds = \int_B \text{grad } u_0 \cdot \text{grad } v dx = \int_T u_0 g ds,$$

\ddagger The particular choice of d is not essential unless stated otherwise.

which proves the *reciprocity principle*

$$\langle f, \Lambda_0 g \rangle_{\mathcal{L}^2(T)} = \langle \Lambda_0 f, g \rangle_{\mathcal{L}^2(T)}.$$

In other words, the operator Λ_0 is selfadjoint, and the same holds for Λ , too. Moreover, we have from (3.1)

$$\begin{aligned} \langle f, (\Lambda - \Lambda_0)f \rangle_{\mathcal{L}^2(T)} &= \int_T f u \, ds - \int_T f u_0 \, ds = 2J_0(u_0) - 2J(u) \\ &\geq 2J_0(u_0) - 2J(u_0) = \int_{\Omega} |\text{grad } u_0|^2 \, dx. \end{aligned}$$

This shows that $\Lambda - \Lambda_0$ is positive, i.e.,

$$\langle f, (\Lambda - \Lambda_0)f \rangle_{\mathcal{L}^2(T)} > 0 \quad \text{for all } f \in \mathcal{L}_{\diamond}^2(T) \setminus \{0\}. \quad (3.2)$$

We emphasize that Λ and Λ_0 both are compact operators (they are, in fact, Hilbert-Schmidt operators) because either of them has a continuous extension to an operator which maps $H_{\diamond}^{-1/2}(T)$ to $H_{\diamond}^{1/2}(T)$, where

$$H_{\diamond}^{\pm 1/2}(T) = \{f \in H^{\pm 1/2}(T) : \int_T f(s) \, ds = 0\}.$$

Here, $H^{\pm 1/2}(T)$ denote the standard Sobolev spaces on T . It follows that $\Lambda - \Lambda_0$ is a compact operator with a trivial null space, and with a range space which is dense in $\mathcal{L}_{\diamond}^2(T)$. As a consequence, we have an orthonormal basis $\{v_k\}$ of eigenfunctions of $\Lambda - \Lambda_0$ with associated eigenvalues λ_k , which we assume to be in nonincreasing order. By virtue of (3.2) these eigenvalues are all positive and, since $\Lambda - \Lambda_0$ is compact, they converge to zero for $k \rightarrow \infty$.

This spectral decomposition can be utilized to define positive powers of $\Lambda - \Lambda_0$, i.e.

$$(\Lambda - \Lambda_0)^{\nu} : \begin{cases} \mathcal{L}_{\diamond}^2(T) & \rightarrow \mathcal{L}_{\diamond}^2(T), \\ f & \mapsto \sum_{k=1}^{\infty} \lambda_k^{\nu} \langle f, v_k \rangle_{\mathcal{L}^2(T)} v_k, \end{cases} \quad (3.3)$$

and a function $h \in \mathcal{L}_{\diamond}^2(T)$ belongs to the range of $(\Lambda - \Lambda_0)^{\nu}$, denoted by $\mathcal{R}(\Lambda - \Lambda_0)^{\nu}$, if and only if the series

$$\sum_{k=1}^{\infty} \lambda_k^{-\nu} \langle h, v_k \rangle_{\mathcal{L}^2(T)} v_k$$

converges in $\mathcal{L}^2(T)$. The latter is the case if and only if the expansion coefficients are square summable, i.e.,

$$\sum_{k=1}^{\infty} \lambda_k^{-2\nu} \langle h, v_k \rangle_{\mathcal{L}^2(T)}^2 < \infty. \quad (3.4)$$

This is the so-called *Picard criterion*. Note that $\lambda_k^{-2\nu} \rightarrow \infty$ for $k \rightarrow \infty$, so (3.4) will diverge for a generic function $h \in \mathcal{L}_{\diamond}^2(T)$. In fact, (3.3) and (3.4) imply that all positive powers of $\Lambda - \Lambda_0$ are compact with dense range in $\mathcal{L}_{\diamond}^2(T)$, and the range spaces increase with decreasing exponent ν .

3.2. The range of $(\Lambda - \Lambda_0)^{1/2}$

Consider once again the difference of the boundary potentials $h = g - g_0 = (\Lambda - \Lambda_0)f$ associated with an input current $f \in \mathcal{L}_\diamond^2(T)$ in (2.2) and (2.3). This function h is the trace of a harmonic potential $w = u - u_0$ in $B \setminus \overline{\Omega}$, which solves the Cauchy problem (2.5). Alternatively, we can view w as the solution of a boundary value problem, namely

$$\Delta w = 0 \quad \text{in } B \setminus \overline{\Omega}, \quad \frac{\partial w}{\partial \nu} = 0 \quad \text{on } T, \quad \frac{\partial w}{\partial \nu} = \varphi \quad \text{on } \Gamma, \quad (3.5)$$

where $\varphi = \varphi_f = \partial(u - u_0)/\partial \nu$ on Γ . Note that φ_f is well-defined in $H_\diamond^{-1/2}(\Gamma)$, cf., e.g., [13, Ch. VII, §1, Lemma 1], and hence there is a unique solution of (3.5) in the space $H_\diamond^1(B \setminus \overline{\Omega})$. Associated with the boundary value problem (3.5) is the operator

$$L : \begin{cases} \mathcal{L}_\diamond^2(\Gamma) & \rightarrow \mathcal{L}_\diamond^2(T), \\ \varphi & \mapsto w|_T, \end{cases} \quad (3.6)$$

which takes Neumann data on Γ (with vanishing mean), and maps them onto the associated Dirichlet values on T . In particular, we note for later use that

$$h = g - g_0 = L\varphi_f, \quad (3.7)$$

and that L is injective. The latter follows again from the uniqueness of the solution of the Cauchy problem (2.5): for if $w|_T = L\varphi = 0$ for some $\varphi \in \mathcal{L}_\diamond^2(\Gamma)$ then w , and hence φ , must vanish everywhere.

An easy computation reveals that the adjoint operator L^* is defined via the solution of the adjoint problem

$$\Delta v = 0 \quad \text{in } B \setminus \overline{\Omega}, \quad \frac{\partial v}{\partial \nu} = \psi \quad \text{on } T, \quad \frac{\partial v}{\partial \nu} = 0 \quad \text{on } \Gamma, \quad (3.8)$$

through

$$L^* : \begin{cases} \mathcal{L}_\diamond^2(T) & \rightarrow \mathcal{L}_\diamond^2(\Gamma), \\ \psi & \mapsto v|_\Gamma. \end{cases}$$

Note that (3.8) coincides with the boundary value problem (2.1), (2.2), and hence

$$L^*f = u|_\Gamma. \quad (3.9)$$

The same argument as above can be used to see that L^* is injective, and hence, that the range of L is dense in $L_\diamond^2(T)$.

The operator L has a continuous extension to $H_\diamond^{-1/2}(\Gamma)$, and from (3.7) and (2.4) we find $\Lambda - \Lambda_0 = LU$ for some continuous operator

$$U : \begin{cases} \mathcal{L}_\diamond^2(T) & \rightarrow H_\diamond^{-1/2}(\Gamma), \\ f & \mapsto \varphi_f. \end{cases}$$

Using the fact that $\Lambda - \Lambda_0$ is selfadjoint we conclude that there exists a factorization

$$\Lambda - \Lambda_0 = LDL^* \quad (3.10)$$

with a symmetric operator $D : \mathcal{L}_\diamond^2(\Gamma) \rightarrow \mathcal{L}_\diamond^2(\Gamma)$ in the middle. The operator D turns out to be unbounded and only densely defined: in fact, in [4] it has been shown that D is an isomorphism from $H_\diamond^{1/2}(\Gamma)$ onto $H_\diamond^{-1/2}(\Gamma)$ with

$$\langle \varphi, D^{-1}\varphi \rangle_{\mathcal{L}_\diamond^2(\Gamma)} \geq c \|\varphi\|_{H_\diamond^{-1/2}(\Gamma)}^2 \quad \text{for all } \varphi \in H_\diamond^{-1/2}(\Gamma). \quad (3.11)$$

Now, let $z \in \Omega$ be fixed and H_z be the modified dipole potential (2.8). Then H_z is harmonic and C^∞ in $B \setminus \overline{\Omega}$, has a well-defined flux $\varphi_z \in H_\diamond^{-1/2}(\Gamma)$ on Γ , and its trace h_z on T satisfies

$$h_z = L\varphi_z, \quad \varphi_z = \frac{\partial H_z}{\partial \nu} \Big|_\Gamma. \quad (3.12)$$

It follows that

$$\begin{aligned} \langle h_z, (\Lambda - \Lambda_0)^{-1} h_z \rangle_{\mathcal{L}_\diamond^2(T)} &= \langle L^{-1} h_z, D^{-1} L^{-1} h_z \rangle_{\mathcal{L}_\diamond^2(T)} \\ &\leq \|D^{-1}\|_{H_\diamond^{-1/2}(\Gamma) \rightarrow H_\diamond^{1/2}(\Gamma)} \|\varphi_z\|_{H_\diamond^{-1/2}(\Gamma)}^2 \end{aligned}$$

is well-defined and finite. Expanding h_z with respect to the eigenfunctions v_k of $\Lambda - \Lambda_0$ this establishes (3.4) for $h = h_z$ and $\nu = 1/2$, i.e.,

$$h_z \in \mathcal{R}(\Lambda - \Lambda_0)^{1/2}.$$

Vice versa it follows from (3.11) that if $h_z \in \mathcal{R}(\Lambda - \Lambda_0)^{1/2}$ then

$$\begin{aligned} \|L^{-1} h_z\|_{H_\diamond^{-1/2}(\Gamma)}^2 &\leq \frac{1}{c} \langle L^{-1} h_z, D^{-1} L^{-1} h_z \rangle_{\mathcal{L}_\diamond^2(\Gamma)} \leq \frac{1}{c} \langle h_z, (\Lambda - \Lambda_0)^{-1} h_z \rangle_{\mathcal{L}_\diamond^2(T)} \\ &= \frac{1}{c} \|(\Lambda - \Lambda_0)^{-1/2} h_z\|_{\mathcal{L}_\diamond^2(T)}^2 < \infty, \end{aligned}$$

i.e., h_z is the trace of a function $w \in H_\diamond^1(B \setminus \overline{\Omega})$ satisfying (3.5) for some $\varphi \in H_\diamond^{-1/2}(\Gamma)$. Since w also satisfies the Cauchy problem (2.5) with $h = h_z$, i.e.

$$\Delta w = 0, \quad w = h_z \quad \text{on } T, \quad \frac{\partial w}{\partial \nu} = 0 \quad \text{on } T, \quad (3.13)$$

it follows that $w = H_z$ on $B \setminus (\overline{\Omega} \cup \{z\})$. As the singularity of H_z is too strong to belong to H^1 in a neighborhood of z we conclude that $z \in \Omega$.

In summary, we have shown that

$$z \in \Omega \quad \text{if and only if} \quad h_z \in \mathcal{R}(\Lambda - \Lambda_0)^{1/2}, \quad (3.14)$$

and this is our key result that opens the door for a variety of algorithms to solve the cavity problem, as we shall describe in the remainder of this paper.

4. A numerical implementation of the factorization method

Using (3.14) we are in the position to improve upon the preliminary algorithm from the end of Section 2. To this end we overlay B with a rectangular grid, and for each grid point z we check whether h_z of (2.9) belongs to $\mathcal{R}(\Lambda - \Lambda_0)^{1/2}$ or not for some direction d . By virtue of (3.14) we thus obtain a discrete set of points approximating the set of cavities Ω . There are some critical technical details, though, see [6], to be described below.

To this end we shall concentrate ourselves on the case where B is the unit disk in \mathbb{R}^2 . Only in Subsections 4.3 and 4.4 we briefly comment on more general (2D) cases. Numerical examples will be included for all items that we discuss, and further numerical results can be found in [6]. Besides, our algorithm can be run on the internet [5] for test cases which can be composed individually. If not mentioned otherwise, the numerical results use a boundary element method with trigonometric ansatz functions to simulate the data. In this implementation the outer boundary T is discretized with 192 collocation points, the inner boundaries $\partial\Omega_j$ with 70 points each. We approximate the eigenvalues of $\Lambda - \Lambda_0$ by the associated Ritz

values, cf., e.g., Stewart [34], i.e. the nonzero eigenvalues of the Galerkin projection $P(\Lambda - \Lambda_0)P^*$, where $P = P^*$ denotes the \mathcal{L}^2 -orthogonal projector onto the span of the 191 trigonometric ansatz functions. The corresponding eigenvectors (Ritz vectors) are taken as approximations for the eigenvectors of $\Lambda - \Lambda_0$.

4.1. The computation of h_z

For a fast method it is essential to compute h_z without solving the differential equations for v_z with individual boundary values (2.7) for each grid point z . Fortunately, it is not the potential H_z but only its trace on T which enters the range criterion (3.14). According to (2.8) the trace of H_z splits into the trace of D_z which is known, cf. (2.6), and the trace of v_z . The latter can be rewritten using the operator Λ_0 , since v_z is harmonic in B and its Neumann boundary values are known, cf. (2.7). Since we assume Λ_0 to be available, it follows that h_z can be evaluated efficiently with the formula

$$h_z = D_z|_T - \Lambda_0 \frac{\partial D_z}{\partial \nu} \Big|_T. \quad (4.1)$$

While (4.1) holds for arbitrary domains $B \subset \mathbb{R}^n$ it simplifies substantially in the unit disk case. There we have the explicit expression

$$h_z = 2D_z|_T = \frac{1}{\pi} \frac{(z-x) \cdot d}{|z-x|^2}, \quad (4.2)$$

cf. [4].

4.2. The numerical range criterion

Since $\Lambda - \Lambda_0$ is a compact operator the correct way of implementing (3.14) is via the Picard criterion (3.4), i.e., the series (3.4) has to be checked for convergence. As only finitely many terms of this series are known (and those only approximately) we have to extrapolate the result of this summation. Fortunately, this is comparatively easy for the cavity problem, since the eigenvalues λ_k exhibit exponential decay, and so do the squared norms of the eigencomponents, $\langle h_z, v_k \rangle_{\mathcal{L}^2}^2$. Therefore we proceed as follows: For some m_0 we determine average decay parameters c and q from

$$\log \lambda_k \approx c + k \log q, \quad k = 1, \dots, m_0, \quad (4.3a)$$

using linear regression, and in the same way we compute for each grid point z parameters γ_z and ϱ_z such that

$$\log \langle h_z, v_k \rangle^2 \approx \gamma_z + k \log \varrho_z, \quad k = 1, \dots, m_0. \quad (4.3b)$$

On the basis of these approximations we get

$$\sum \lambda_k^{-1} \langle h_z, v_k \rangle^2 \sim \sum \left(\frac{\varrho_z}{q} \right)^k$$

which suggests to determine an approximation $\tilde{\Omega}$ of Ω using the numerical range criterion

$$z \in \tilde{\Omega} \quad \text{if and only if} \quad \varrho_z < q. \quad (4.4)$$

We recommend, however, to modify (4.3) slightly for the following reason. In all our numerical computations the Ritz values of $\Lambda - \Lambda_0$ essentially came in close pairs. We found it to be of advantage to accumulate the information from each of these pairs in one number by replacing the two eigenvalues by their geometric mean and the two

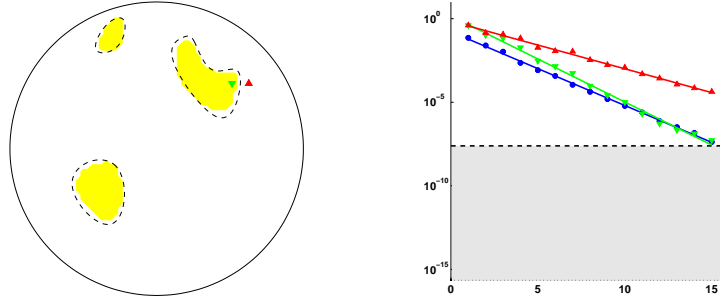


Figure 1. Reconstruction of a phantom and illustration of (4.3) for two test points; $m_0 = 15$.

corresponding eigencomponents by their sum. In the sequel, the terms in (4.3) and all figures which illustrate our results must be understood in this sense.

Consider the test phantom in Figure 1 which will serve as our benchmark example in the following. There are three cavities indicated by dashed lines and two test points for the ease of illustration: z_1 , marked by a triangle pointing down, is within one of the inclusions while z_2 (triangle pointing up) is outside the inclusions. The right-hand side plot demonstrates the result of the linear regression for the Ritz values (blue bullets) and the eigencomponents (4.3b) of the two test points. The green line corresponding to z_1 is steeper than the blue line, hence $z_1 \in \tilde{\Omega}$ by virtue of (4.4). The red line associated with z_2 is not as steep; according to our criterion (4.4) we deduce that $z_2 \notin \tilde{\Omega}$. The yellow region in the left-hand side plot shows the entire reconstruction $\tilde{\Omega}$. This result is based on $m_0 = 15$ (averaged) eigenvalues of $\Lambda - \Lambda_0$, as indicated by the dashed line in the right-hand side plot. For this particular phantom, a greater value of m_0 would not really improve the reconstruction.

4.3. General bounded and simply connected domains $B \subset \mathbb{R}^2$

So far we have focused our attention to the case where B is the unit disk in \mathbb{R}^2 . This can be justified by the fact that any two-dimensional bounded and simply connected domain B' can be mapped conformally onto the unit disk. Let ψ be the conformal mapping which takes the unit disk B onto B' and let ϕ be its inverse. We assume that T' is so smooth that ψ and ϕ have continuous extensions onto the boundaries T and T' of B and B' , respectively. With abuse of notation we will consider ϕ and ψ as complex-valued holomorphic functions and identify \mathbb{R}^2 with \mathbb{C} whenever appropriate.

Any cavity $\Omega'_j \subset B'$ is mapped by ϕ onto a domain $\Omega_j = \phi(\Omega'_j) \subset B$. Once we are able to find $\Omega = \bigcup \Omega_j$ we thus obtain $\Omega' = \psi(\Omega)$. As we have already explained, Ω can be approximated numerically if the Neumann-Dirichlet operator Λ associated with the domain $B \setminus \overline{\Omega}$ is known. Let $f \in \mathcal{L}^2_\circ(T)$ be a current on the unit circle and u be the solution of the associated boundary value problem (2.1), (2.2). Then $v = u \circ \phi$ is a harmonic function on $B' \setminus \overline{\Omega'}$ with flux

$$\frac{\partial v}{\partial \nu} = |\phi'| \frac{\partial u}{\partial \nu} \circ \phi \quad \text{on } T' \cup \partial\Omega',$$

where $|\phi'|$ denotes the modulus of the complex valued derivative of ϕ . It follows that

$$\frac{\partial v}{\partial \nu} = 0 \quad \text{on } \partial\Omega', \quad \frac{\partial v}{\partial \nu} = |\phi'| f \circ \phi \quad \text{on } T',$$

and hence,

$$\Lambda f = u|_T = g' \circ \psi,$$

where $g' = v|_{T'}$ is the boundary potential on T' associated with the boundary current $f' = |\phi'| f \circ \phi$.

In this way we can transform the given Neumann-Dirichlet data for $B' \setminus \overline{\Omega'}$ to Neumann-Dirichlet data associated with the boundary value problem (2.1), (2.2), and use the technique described before to reconstruct Ω and $\Omega' = \psi(\Omega)$. To implement this algorithm we need to compute the conformal map ψ and the restriction of the inverse map ϕ to the boundary T' , as is described for example in Henrici [20].

An alternative implementation has been suggested in [6]. There, all computations are carried out in B' (or $B' \setminus \overline{\Omega'}$), no computations are transferred to the unit disk. Because of that, the transform ψ is not required. On the other hand, with this approach one needs to know the test functions h'_z for the individual grid points in B' . Again, conformal mapping theory can be used to obtain h'_z without solving a boundary value problem for v_z of (2.8) and without using (4.1). Rather, it can be shown that in this case

$$h'_z = h_{\phi(z)} \circ \phi + \alpha_z,$$

where the real parameter α_z has to be tuned to satisfy $\int_{T'} h'_z ds = 0$. Note, however, that α_z is irrelevant for our purposes because α_z has no impact on the inner products $\langle h'_z, v_k \rangle_{\mathcal{L}^2(T')}$ required for (4.3b). We refer to [6] for numerical examples.

4.4. Numerical results for the half space $B \subset \mathbb{R}^2$

Recently Schappel [31] extended some of our results to the half space geometry in \mathbb{R}^2 , which is a prototype of an unbounded domain where data are only accessible on one side of the object. As such the setting is similar to the one to be discussed in Section 7 below.

Let B be a two-dimensional half space, i.e. the upper half plane in a (ξ, η) -coordinate system, and $\Omega = \bigcup \Omega_j \subset B$ be the union of insulating and bounded cavities as before. While T is now the entire ξ -axis, we shall assume that the electrode system has only finite extent, i.e., currents are only applied on some bounded interval $I \subset T$. More precisely, let

$$f \in \mathcal{L}^2_{\diamond}(I) = \{f \in \mathcal{L}^2(I) : \int_I f(\xi) d\xi = 0\},$$

and modify the boundary condition on T in (2.2) and (2.3) to

$$\frac{\partial u}{\partial \nu} = f \quad \text{on } I, \quad \frac{\partial u}{\partial \nu} = 0 \quad \text{on } T \setminus I.$$

With this modification, both boundary value problems have unique solutions u and u_0 , which tend to zero as $|x| \rightarrow \infty$ and satisfy

$$\int_{B \setminus \overline{\Omega}} |\text{grad } u|^2 dx < \infty, \quad \int_B |\text{grad } u_0|^2 dx < \infty.$$

If measurements of the potentials are also restricted to the interval I we can shift them to have vanishing mean (again denoted by u and u_0), and thus obtain the local Neumann-Dirichlet operators

$$\Lambda : \begin{cases} \mathcal{L}^2_{\diamond}(I) & \rightarrow \mathcal{L}^2_{\diamond}(I), \\ f & \mapsto u|_I, \end{cases} \quad \text{and} \quad \Lambda_0 : \begin{cases} \mathcal{L}^2_{\diamond}(I) & \rightarrow \mathcal{L}^2_{\diamond}(I), \\ f & \mapsto u_0|_I. \end{cases}$$

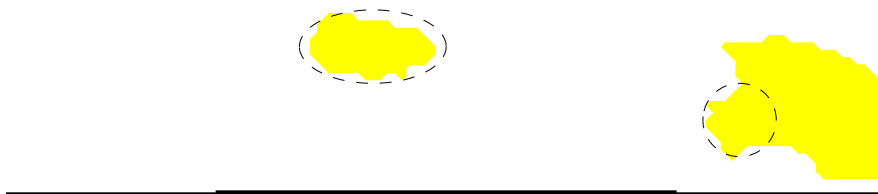


Figure 2. Reconstruction of two cavities in the half plane.

It can then be shown that a point z belongs to Ω , if and only if the restriction $h_z|_I$ of our test function—shifted by a constant so that it belongs to $\mathcal{L}_\circ^2(I)$ —is in $\mathcal{R}(\Lambda - \Lambda_0)^{1/2}$. See Section 7 for a similar argument in the case of a bounded domain B . We mention that h_z here has the same specific form (4.2) as in the unit disk case.

We refer to Figure 2 for a preliminary numerical result for this setting. It shows a sketch of a phantom consisting of an ellipse and a circle and, in yellow, its reconstruction from data corresponding to simulated measurements taken on the interval highlighted by a thick line. For this plot $m_0 = 9$ (averaged) eigenvalues have been used, and no noise has been added. Note that the circle is aside of the interval where measurements are taken. It therefore comes as no big surprise that this circle ‘casts a shadow’ onto the region behind it. However, there are more subtle techniques to reduce this shadow, or even get rid of it. Some of them are described in [31], and we shall not dwell on this here. We only mention that they are related to an appropriate choice of one or several dipole axes d for the test functions h_z . For the above reconstruction d has been fixed to point downwards vertically.

5. Practical considerations

Usually in practice, data $g_i = \Lambda f_i$, $i = 1, \dots, m$, are given for some linearly independent sequence of boundary currents. Typically, m is a small number, e.g., $m = 32$. Then one should first project the boundary potentials g_i onto the span of the boundary currents, and store the corresponding expansion coefficients in a matrix $A \in \mathbb{R}^{m \times m}$. We shall assume that the boundary currents from an orthonormal sequence in which case this matrix is symmetric up to measurement errors. Note that A is the matrix representation (corresponding to the coordinates for the basis $\{f_i\}$) of the Galerkin projection $P(\Lambda - \Lambda_0)P^*$, where P denotes now the orthogonal projector onto the span of the given currents.

Then one needs to store the boundary potentials $\Lambda_0 f_i$ for $i = 1, \dots, m$ in a similar way. If possible, these potentials should be measured with the same measuring device using a homogeneous phantom. Otherwise, Λ_0 has to be simulated numerically by solving the associated Neumann boundary value problems (2.3) for $f = f_i$, $i = 1, \dots, m$. This has to be done only once and for all, and hence this work load can be ignored further on.

Since m is small, the spectral decomposition of A is rather cheap to compute. However, these eigenvalues usually only approximate the dominant eigenvalues of $\Lambda - \Lambda_0$. For example, to have good approximations of all 15 (averaged) eigenvalues of $\Lambda - \Lambda_0$ used in Figure 1, and to achieve a similar reconstruction of this phantom, it would be necessary to measure data for the first 2×37 sine and cosine frequencies. Vice versa, with only $m = 32 = 2 \times 16$ sine and cosine frequencies the algorithm

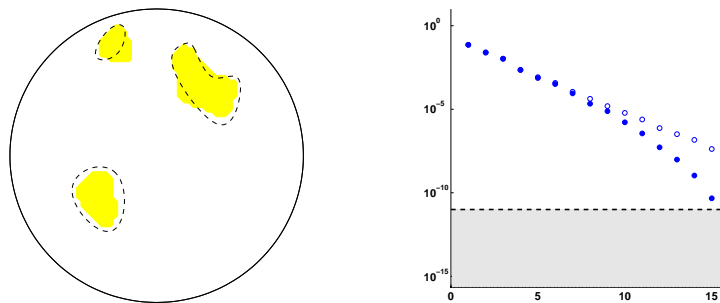


Figure 3. Reconstruction with 32 currents imposed; $m_0 = 15$.

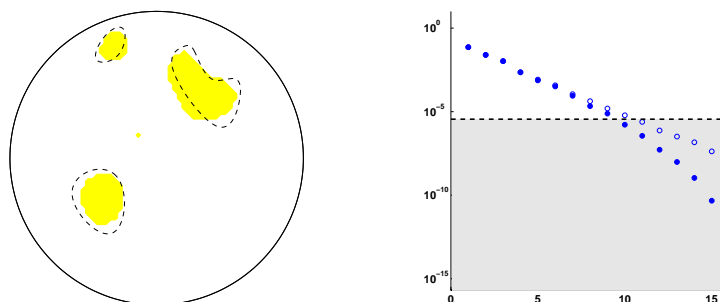


Figure 4. Reconstruction with 32 currents imposed; $m_0 = 9$.

described in Section 4 gives inferior results.

For this latter situation reconstructions of our phantom are shown in Figures 3 and 4. In Figure 3 the same number of eigenvalues has been used as in Figure 1, although it is obvious from the right-hand side plot that only seven of the computed eigenvalues are reasonable approximations of true eigenvalues (included as circles for comparison purposes), and although the smaller eigenvalues appear to decay superlinearly.

Intuitively, a restriction to $m_0 = 9$ eigenvalues should be more reliable since only those appear to have linear decay, essentially. This is what we did for Figure 4. It turns out, however, that both reconstructions can compete. While the reconstruction of the tiny inclusion is somewhat smeared in Figure 3, an isolated spot went astray near the center of the disk in Figure 4.

In any case, if data for m boundary currents are given, only much fewer ($m_0 < m$) eigenvalues can be used in general. This gets even worse if the data are noisy which will always be the case in practice. In this situation we obtain a matrix A^δ instead of A with

$$\frac{\|A - A^\delta\|_F}{\|A\|_F} \leq \delta. \quad (5.1)$$

Here $\|\cdot\|_F$ denotes the Frobenius norm and δ is related to the noise level. If A^δ happens to be nonsymmetric then we can replace it by its symmetric part without violating (5.1). We can actually go one step further and replace negative eigenvalues of A^δ by their absolute value without violating (5.1) because A is positive definite. Therefore we can assume in the sequel that A^δ is symmetric positive semidefinite. By

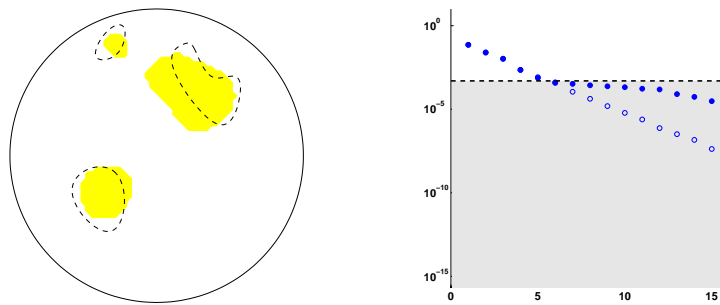


Figure 5. Reconstruction with 0.1% noise; $m_0 = 5$.

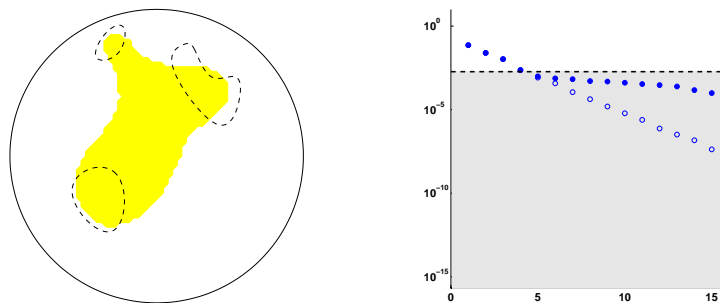


Figure 6. Reconstruction with 0.2% noise; $m_0 = 4$.

the Wielandt-Hoffman Theorem the eigenvalues of A^δ are perturbations of those of A , each perturbation being at most $\delta\|A\|_F$ in size. This means that eigenvalues of $\Lambda - \Lambda_0$ which are larger than $\delta\|A\|_F$ will go through a comparatively small relative change by virtue of (5.1), whereas eigenspaces corresponding to eigenvalues below $\delta\|A\|_F$ may be completely deteriorated.

As a consequence, m_0 has to be restricted somewhat further in the presence of noise. For an example consider Figure 5 which has been obtained with synthetic (random) noise added upon A such that $\delta = 10^{-3}$ (0.1% noise). In this example, only $m_0 = 5$ eigenvalues can be used but the reconstruction is not too bad because all three components of Ω have been detected. Of course, the quality of the reconstruction is not as good as in Figure 4.

It turns out, however, that in this example and with this algorithm five eigenvalues are strictly necessary to distinguish between the three components of Ω . A reconstruction based on only four eigenvalues—as in Figure 6 with $\delta = 2 \cdot 10^{-3}$ —is always connected, regardless of the noise level, smearing out the three components to one big one. We will see in the next section how we can, to a certain extent, do better in this case.

It is important to note, though, that the index of truncation, m_0 , is usually apparent from a plot of the eigenvalues of A , since the eigenvalues typically reach a certain plateau beyond the optimal value of m_0 , compare the right-hand side plots of Figures 5 and 6. In other words, no information about the noise level is really required for the reconstruction.

6. The MUSIC connection

MUSIC is an imaging technique introduced by Devaney [14] to find a finite number of point scatterers from waves transmitted and received from a given set of antennas. In the MUSIC algorithm the point scatterers are detected by a range criterion which has similarities to (3.14) but is finite-dimensional. In fact, it was Cheney [9] and subsequently Kirsch [23] who observed and elaborated on the connection with (3.14).

A similar result holds for electrical impedance tomography, where infinitesimally small cavities take the role of the point scatterers, see [8]. Let B be the unit disk, and $z_j \in B$, $j = 1, \dots, p$, be the centers of small disk-shaped cavities Ω_j with radius εr_j , i.e. $\Omega_j = z_j + \varepsilon r_j B$. Here, $r_j > 0$ may be different for each cavity, but $\varepsilon > 0$ is a common scaling parameter. We assume ε to be so small that the sets $\overline{\Omega}_j$ are mutually disjoint and contained in B . Then the boundary value problem (2.1), (2.2) has a unique solution u_ε whose boundary values tend to $u_0|_T$ for $\varepsilon \rightarrow 0$. Moreover, Friedman and Vogelius [17] gave an asymptotic expansion of $u_\varepsilon|_T$ as $\varepsilon \rightarrow 0$ which can be used to prove that the associated Neumann-Dirichlet operators $\Lambda_\varepsilon : \mathcal{L}_\diamond^2(T) \rightarrow \mathcal{L}_\diamond^2(T)$ converge to Λ_0 with

$$\Lambda_\varepsilon - \Lambda_0 = \varepsilon^2 K + o(\varepsilon^2), \quad \varepsilon \rightarrow 0, \quad (6.1)$$

where K is a rank $2p$ operator, the range of which is spanned by the functions h_{z_j} , $j = 1, \dots, p$, of (4.2) with arbitrary unit vectors $d \in \mathbb{R}^2$, cf. [8, Proposition 2.1].

It follows that $\mathcal{R}(\Lambda_\varepsilon - \Lambda_0)$ is (essentially) the same as the range of K , and hence, essentially finite-dimensional. This has a number of important consequences. First of all, it implies that $\mathcal{R}(\Lambda_\varepsilon - \Lambda_0)$ and $\mathcal{R}(\Lambda_\varepsilon - \Lambda_0)^{1/2}$ coincide within this approximation so that we can modify our test (3.14) and search for points $z \in B$ with $h_z \in \mathcal{R}(\Lambda_\varepsilon - \Lambda_0)$. Second, instead of using the Picard criterion to check an infinite-dimensional range condition we can resort to more familiar techniques from numerical linear algebra, and compute the angle θ_z between h_z and the range of $\Lambda_\varepsilon - \Lambda_0$: If P denotes the orthoprojector onto a finite dimensional space \mathcal{R} then the angle θ between h and \mathcal{R} is defined to be

$$\cot \theta = \|Ph\| / \|(I - P)h\|.$$

With the data we are given, we may replace $\mathcal{R}(K)$ by \mathcal{R}^δ , where \mathcal{R}^δ is the span of those m_0 Ritz vectors of $\Lambda - \Lambda_0$ whose Ritz values are greater than the noise level δ . Denoting by P^δ the orthogonal projector onto \mathcal{R}^δ we thus approximate

$$\cot \theta_z \approx \|P^\delta h_z\| / \|(I - P^\delta)h_z\|, \quad (6.2)$$

where

$$\|P^\delta h_z\|^2 = \sum_{k=1}^{m_0} \langle h_z, v_k \rangle^2 \quad \text{and} \quad \|(I - P^\delta)h_z\|^2 = \sum_{k=m_0+1}^m \langle h_z, v_k \rangle^2. \quad (6.3)$$

A color-coded plot of $\log \cot \theta_z$ can then be used to visualize the result and to find the approximate location of the cavities, cf. Figure 7.

As a consequence, the MUSIC algorithm gives only a rough idea of possible locations of the cavities, it does not allow a binary test whether some point z belongs to the cavity or not, as does the factorization method. On the other hand, the computation (6.2), (6.3) is much less susceptible to data errors than the numerical range criterion based on the regression parameters q and q_z of (4.3). This is nicely illustrated in Figure 7. The first two plots show the MUSIC reconstructions corresponding to the same data as the reconstructions in Figures 5 and 6, and the

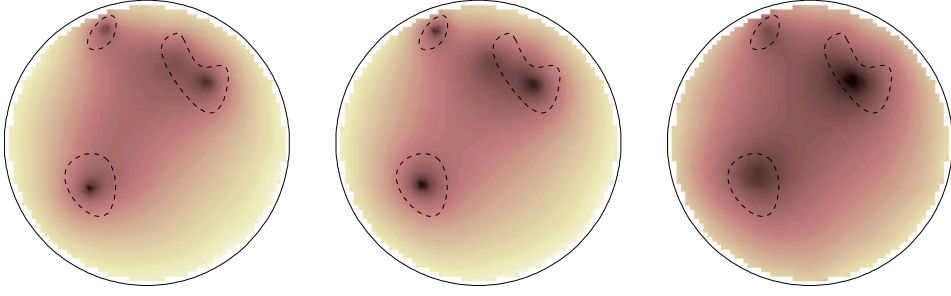


Figure 7. MUSIC reconstructions with noise levels $\delta = 10^{-3}$, $2 \cdot 10^{-3}$, and $2 \cdot 10^{-2}$.

same parameters $m_0 = 5$ and $m_0 = 4$, respectively. These reconstructions do not really show the shape of the cavities but they clearly demonstrate that there are three of them, and where they are. The same is true for the third plot in Figure 7, which uses only $m_0 = 3$ eigenvalues and is based on data with 2% noise. In other words, for this example, MUSIC can handle up to twenty times as much noise as the factorization method.

Our numerical experience indicates that the number m_0 of (averaged) eigenvalues must not be smaller than the number of cavities (see also [8]). For this example, three eigenvalues are therefore a minimal requirement to obtain useful reconstructions, and this limitates the noise level to be at most 2%.

7. Limited angle data

The algorithms discussed so far can be extended to various settings where only restricted data are accessible. Let us assume that the potential difference $h = g - g_0$ is mapped by some bounded and surjective observation operator

$$P : \begin{cases} \mathcal{L}_\diamond^2(T) & \rightarrow Z, \\ h & \mapsto Ph, \end{cases} \quad (7.1)$$

onto an appropriate Hilbert space Z , which is our data space. Then it is crucial for our analysis whether P is injective on the subspace Y of real analytic functions on T with vanishing mean. Recall that a function from the range of L is the trace $w|_T$ of a harmonic function w with zero flux on T , cf. (3.5), (3.6). Therefore w has a harmonic extension into a neighborhood of the unit circle so that $w|_T$ is a real analytic function, cf., e.g., [13, Ch. II, §2]. In other words, we have the inclusion

$$\mathcal{R}(L) \subset Y \subset \mathcal{L}_\diamond^2(T). \quad (7.2)$$

Moreover, $h_z \in Y$ for any $z \in B$, as is obvious from (4.2).

In the remainder of this section we assume that P is injective on Y . The situation will be strikingly different when this assumption fails, as we will see in the following section. Note that if P is injective on Y , then the operator

$$PL : H_\diamond^{-1/2}(\Gamma) \rightarrow Z$$

is also injective and has an (unbounded) inverse $(PL)^{-1}$. It follows from (3.10) that in this case

$$(P(\Lambda - \Lambda_0)P^*)^{-1} = (PLD(PL)^*)^{-1} = (PL)^{-*}D^{-1}(PL)^{-1}.$$

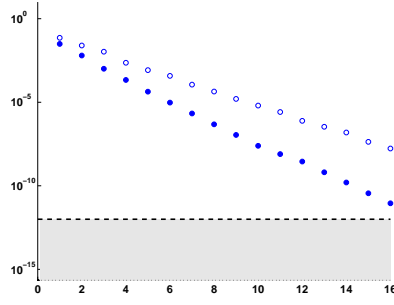


Figure 8. Eigenvalues for full circle data and limited angle data (120°).

Furthermore, if $z \in \Omega$ so that the potential h_z of (2.9) satisfies $h_z = L\varphi_z$, cf. (3.12), then we obtain as in Section 3 that

$$\begin{aligned} \langle Ph_z, (P(\Lambda - \Lambda_0)P^*)^{-1}Ph_z \rangle &= \langle PL\varphi_z, (PL)^{-*}D^{-1}(PL)^{-1}PL\varphi_z \rangle \\ &= \langle \varphi_z, D^{-1}\varphi_z \rangle \\ &\leq \|D^{-1}\|_{H_\diamond^{-1/2}(\Gamma) \rightarrow H_\diamond^{1/2}(\Gamma)} \|\varphi_z\|_{H_\diamond^{-1/2}(\Gamma)}^2. \end{aligned}$$

However, if $z \notin \Omega$ then $h_z \notin \mathcal{R}(L)$ and hence $Ph_z \notin \mathcal{R}(PL)$ because of the injectivity of P on Y . This implies that

$$Ph_z \in \mathcal{R}(P(\Lambda - \Lambda_0)P^*)^{1/2} \quad \text{if and only if} \quad z \in \Omega. \quad (7.3)$$

To reconstruct Ω we can therefore proceed in much the same way as in the previous sections. We choose m orthonormal elements ψ_1, \dots, ψ_m of Z , use $f_i = P^*\psi_i$ as boundary currents, and expand the measured data in the orthonormal system $\{\psi_i\}$. These expansion coefficients make up the matrix $A \in \mathbb{R}^{m \times m}$, whose eigenvalues and eigenvectors yield Ritz approximations of the eigenvalues and eigenvectors of $P(\Lambda - \Lambda_0)P^*$, which can then be used as before.

An example for such an operator P occurs in the limited angle problem, where data can only be measured on parts of the boundary. Let B be the unit disk in \mathbb{R}^2 and assume that the potential is only measured on an open subset T_0 of the unit circle. Then we denote by

$$Z = \{f \in \mathcal{L}_\diamond^2(T) : f = 0 \text{ a.e. on } T \setminus T_0\}$$

and by P the orthoprojector from $\mathcal{L}_\diamond^2(T)$ onto Z . Note that Ph is determined via

$$Ph(s) = \begin{cases} h(s) - \gamma, & s \in T_0, \\ 0, & s \in T \setminus T_0, \end{cases} \quad \text{with } \gamma = \frac{1}{|T_0|} \int_{T_0} h(s) ds. \quad (7.4)$$

While P is certainly not injective on all of $\mathcal{L}_\diamond^2(T)$, it is injective on Y because of the unique continuation principle for analytic functions. Our assumptions are therefore satisfied.

For obvious reasons the limited angle problem is even more ill-posed than the full data cavity problem. This can also be seen in Figure 8, where the eigenvalues of $P(\Lambda - \Lambda_0)P^*$ (bullets) are compared to those of $\Lambda - \Lambda_0$ (circles). Here, we assume that only one third (120°) of the boundary T is accessible to take measurements. Note that the eigenvalues decay much faster for the limited angle problem, and therefore fewer eigenvalues will carry relevant information in the noisy case.

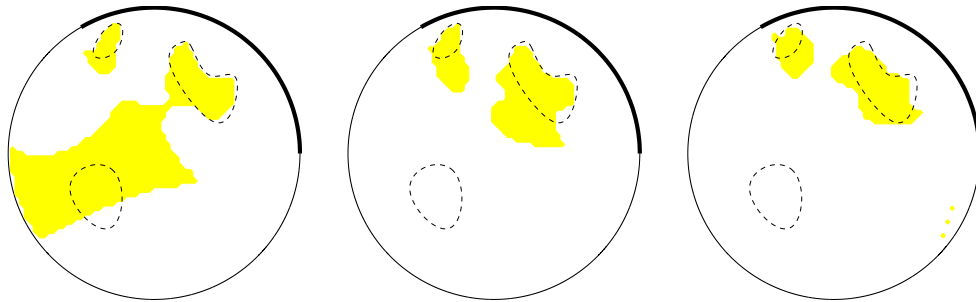


Figure 9. Reconstructions of the test phantom from 120° angle data, with $m_0 = 16, 9,$ and 5 (from left to right).

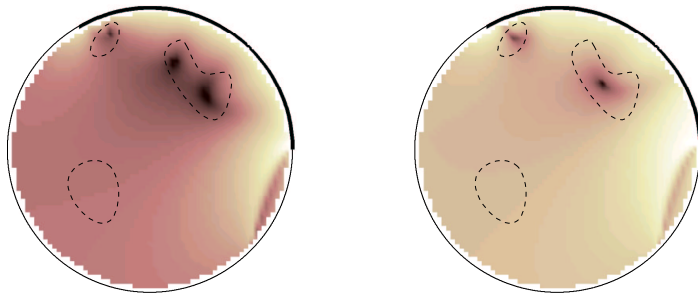


Figure 10. Reconstructions of the test phantom from 120° angle data, with $m_0 = 3$ (see text).

Figure 9 shows the reconstructions of the factorization method for the limited angle case (no noise added), using $m_0 = 16$, $m_0 = 9$, and $m_0 = 5$ (averaged) eigenvalues. The thick line on the boundary is the subset of T where measurements are taken. With five eigenvalues only those two cavities near this subset are visible; the third inclusion is in their shadow region. With an increasing number of eigenvalues the reconstructed domain ‘creeps’ slowly towards the third cavity, and with $m_0 = 16$ eigenvalues the reconstructed domain has almost split into three distinct components.

Figure 10 shows two other reconstructions for the limited angle case, using only $m_0 = 3$ eigenvalues. The left-hand side plot is the MUSIC reconstruction. The right-hand side plot shows the so-called power visualization associated with the factorization method: This is a color-coded plot of the ratio $\log \varrho_z / \log q$ obtained from (4.3). In view of (4.4) the reconstructed domain of the factorization method is the set where this ratio is greater than one. For a general value of this quotient we obtain the following interpretation from the Picard criterion:

$$\frac{\log \varrho_z}{\log q} > \nu \quad \text{if and only if} \quad h_z \in \mathcal{R}(\Lambda - \Lambda_0)^{\nu/2}.$$

(Of course, this is not really an ‘equivalence’ because the values of ϱ_z and q are rough estimates of the actual decay rates of the eigenvalues and the squared eigencomponents.) This plot contains more details than the reconstructions in Figure 9, and gives similar information as the MUSIC reconstruction.

8. Electrode models

When the observation operator P in (7.1) fails to be injective on Y , the test function Ph_z may belong to $\mathcal{R}(P(\Lambda - \Lambda_0)P^*)^{1/2}$ even when $z \notin \Omega$, thus violating (7.3). This situation occurs quite naturally, if not to say always in practice when Z is finite dimensional, e.g. the output of finitely many electrodes. On the other hand, recall that even for the complete data case we represent $\Lambda - \Lambda_0$ only by a finite dimensional Galerkin projection A of dimension $m \times m$, cf. Section 4. Therefore, it is fair to hope that if the dimension of Z is sufficiently large, say m again, then we can proceed as in the continuous regime of Section 4. At least we should be able to use the MUSIC type algorithm of Section 6 since it is adopted to the finite dimensional case.

As an example we consider two electrode models for the data acquisition from the literature. We assume that $m + 1$ electrodes of positive width are attached to the surface of the object, each of which is used to inject a certain amount of electrical current, and to measure one single number as a potential. Since the boundary currents have to sum up to zero we can apply m linearly independent current patterns this way.

8.1. The gap model

In the gap model the current injected through a specific electrode is assumed to have uniform strength on the entire area of the electrode. Thus, if J_ℓ is the total current injected through the ℓ th electrode $E_\ell \subset T$ of size $|E_\ell|$, then the current pattern f in (2.2), (2.3) becomes

$$f = \begin{cases} J_\ell/|E_\ell| & \text{on } E_\ell, \ell = 0, \dots, m, \\ 0 & \text{on } T \setminus \bigcup_{\ell=0}^m E_\ell. \end{cases} \quad (8.1)$$

Furthermore, the measured potential U_ℓ is considered to be the mean of the potential on E_ℓ ,

$$U_\ell = \frac{1}{|E_\ell|} \int_{E_\ell} g \, ds, \quad \ell = 0, \dots, m. \quad (8.2)$$

The gap model has the advantage of being easy to work with mathematically. It immediately applies to our setting (7.1) with an observation operator P which maps the boundary potential g onto the vector

$$[U_\ell]_{\ell=0}^m \subset \mathring{\mathcal{L}}^{m+1} = \{y = [y_0, \dots, y_m] \in \mathring{\mathcal{L}}^{m+1}, \sum_{\ell=0}^m y_\ell = 0\},$$

where the numbers U_ℓ are given by (8.2), properly shifted in order to belong to $\mathring{\mathcal{L}}^{m+1}$. It is easy to verify that the adjoint operator P^* maps the $(m+1)$ -vector $[J_\ell]_{\ell=0}^m \subset \mathring{\mathcal{L}}^{m+1}$ onto the function $f \in \mathcal{L}_\diamond^2(T)$ defined in (8.1).

Of course, since $Z = \mathcal{R}(P)$ is finite-dimensional, P cannot be injective on Y . Therefore the range criterion (3.14) has to be replaced by the weaker statement

$$z \in \Omega \quad \text{implies} \quad Ph_z \in \mathcal{R}(P(\Lambda - \Lambda_0)P^*)^{1/2}.$$

Moreover, the range of the square root $(P(\Lambda - \Lambda_0)P^*)^{1/2}$ coincides with that of $P(\Lambda - \Lambda_0)P^*$ because these operators have finite rank. However, $P(\Lambda - \Lambda_0)P^*$ is a Galerkin approximation of $\Lambda - \Lambda_0$ just as in Section 5, with input currents of the form (8.1). Our numerical results seem to support the argument that for our purposes

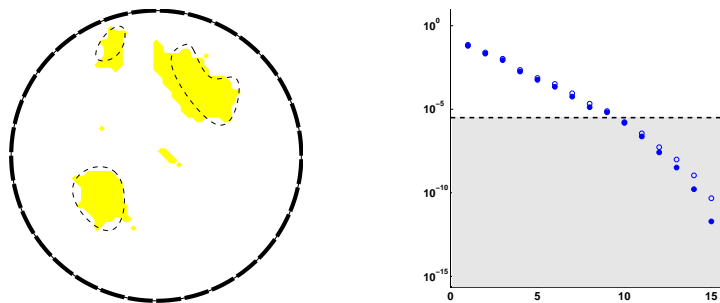


Figure 11. Eigenvalues and reconstruction for the gap model; $m_0 = 9$.

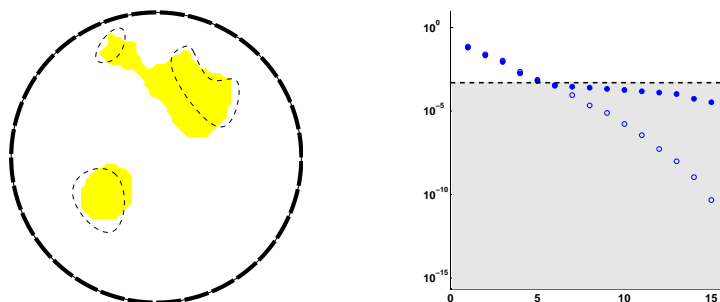


Figure 12. Reconstruction for the gap model with 0.1% noise; $m_0 = 5$.

the gap model is a useful approximation of the continuous case, at least when the electrodes cover large parts of the boundary T .

Motivated by the experimental setup by J. Newell at the Rensselaer Polytechnic Institute [30] we assume that the $m + 1 = 32$ electrodes cover altogether about 87.5% of the boundary of the tank (which is considered to be essentially two dimensional). To achieve in our simulations a sufficient precision of the potentials on and between the electrodes we need a finer discretization of the outer boundary than in the previous sections. As a consequence, we use 24576 unknowns on the boundary, solve the linear equations by block elimination combined with FFT techniques to evaluate the associated single layer potential on T .

Figure 11 compares the eigenvalues for the gap model (bullets), where $m = 31$ discrete trigonometric currents can be and have been injected, with those of the continuous model (circles) using $m = 32$ continuous trigonometric currents. The important dominant eigenvalues appear to be in good agreement. The left-hand side plot shows our reconstruction for the gap model with $m_0 = 9$ eigenvalues, which should be compared with the reconstruction in Figure 4.

Figure 12 shows a reconstruction for noisy gap model data. The relative amount of noise is the same as in Figure 5 for the continuous model, and the number $m_0 = 5$ of admissible eigenvalues is also the same. This particular noise level is just at the edge where the reconstructions start to smear the upper two cavities to one bigger blob. The MUSIC reconstruction for the same data (left plot in Figure 13) is very similar to the one for the continuous problem (see the left-hand side plot in Figure 7), although it shows some fingering artifacts caused by the electrode gaps. Finally, the right-hand

§ In fact, it is this implementation that we have also used for the numerical examples in Section 7.

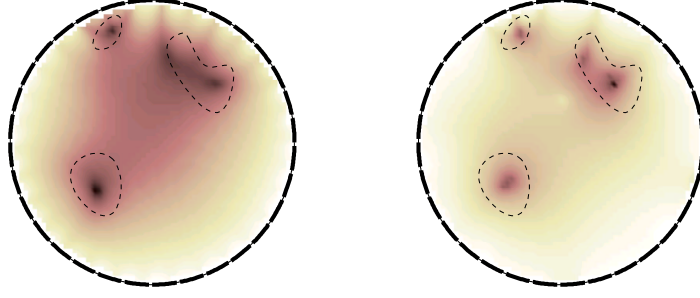


Figure 13. MUSIC reconstruction (left) and power visualization for the gap model with 0.1% noise; $m_0 = 5$.

side plot in Figure 13 is the power visualization of the factorization method that we have introduced in Section 6 (Figure 10). It yields probably the best reconstruction of the three cavities with the gap model in the presence of 0.1% noise.

We conclude that for this example the discrete electrode data seem to carry enough information to justify the application of the ‘continuous theory’. The quality of the reconstruction suffers somewhat because of the discretization but is almost as good as for continuous data.

8.2. The shunt model

More realistic electrode models take into account that metal electrodes are perfectly conducting so that the electrostatic potential for a given input current is always constant along each electrode, i.e.

$$g|_{E_\ell} = \text{const.}, \quad \ell = 0, \dots, m. \quad (8.3)$$

The actual values U_ℓ of these constants are the measured data. For this model it is not possible to prescribe the boundary flux f exactly, only the total flux J_ℓ across E_ℓ is known, namely the amount of current injected through this electrode. In other words, we know that

$$\int_{E_\ell} \frac{\partial u}{\partial \nu} ds = J_\ell, \quad \ell = 0, \dots, m, \quad \frac{\partial u}{\partial \nu} = 0 \quad \text{on } T \setminus \bigcup E_\ell. \quad (8.4)$$

Recall that $\sum_{\ell=0}^m J_\ell = 0$. In addition to (8.4) the electrostatic potential has to satisfy

$$\Delta u = 0 \quad \text{in } B \setminus \overline{\Omega}, \quad \frac{\partial u}{\partial \nu} = 0 \quad \text{on } \Gamma. \quad (8.5)$$

The shunt model (8.3) restricts the set of admissible solutions u of (8.4) and (8.5) to the subspace

$$H_{\diamond, E}^1(B \setminus \overline{\Omega}) = \{u \in H^1(B \setminus \overline{\Omega}), u|_{E_\ell} = \text{const. for } \ell = 0, \dots, m, \sum_{\ell=0}^m u|_{E_\ell} = 0\}.$$

It has been shown in [33] that the boundary value problem (8.4), (8.5) has a unique solution $u \in H_{\diamond, E}^1(B \setminus \overline{\Omega})$. According to the variational principle this potential u minimizes the functional

$$J(v) = \frac{1}{2} \int_{B \setminus \overline{\Omega}} |\text{grad } v|^2 dx - \sum_{\ell=0}^m v|_{E_\ell} J_\ell$$

over $H_{\diamond,E}^1(B \setminus \overline{\Omega})$ and solves the variational equation

$$\int_{B \setminus \overline{\Omega}} \text{grad } u \cdot \text{grad } v \, dx = \sum_{\ell=0}^m v|_{E_\ell} J_\ell \quad (8.6)$$

for all functions $v \in H_{\diamond,E}^1(B \setminus \overline{\Omega})$.

It is not straightforward to apply our theory as it stands to the shunt model because the flux of the potential at the boundary T is unknown and depends on the cavities themselves. Instead we adapt our theory to the weak formulation (8.6). Here, the resistivity matrix R defined by

$$R : \begin{cases} \begin{matrix} \diamond^{m+1} & \rightarrow & \diamond^{m+1}, \\ [J_0, \dots, J_m] & \rightarrow & [U_0, \dots, U_m], \end{matrix} \end{cases} \quad (8.7)$$

where $U_\ell = u|_{E_\ell}$ are the measured potentials, takes over the role of the Neumann-Dirichlet operator Λ in the previous sections. Denoting by R_0 the corresponding resistivity matrix for the homogeneous body, essentially the same argument as in Section 3.1 can be used to see that $R - R_0$ is selfadjoint and positive definite.

Next we are interested in finding a factorization of $R - R_0$ which corresponds to (3.10). To this end we note that the weak form of (3.5) is

$$\int_{B \setminus \overline{\Omega}} \text{grad } w \cdot \text{grad } v \, dx = \int_{\Gamma} \varphi v \, ds, \quad (8.8)$$

valid for all $v \in H_{\diamond,E}^1(B \setminus \overline{\Omega})$. If v is restricted instead to $H_{\diamond,E}^1(B \setminus \overline{\Omega})$ then there is a unique solution $w \in H_{\diamond,E}^1(B \setminus \overline{\Omega})$ of (8.8), and we can define

$$L_E : \begin{cases} \mathcal{L}_{\diamond}^2(\Gamma) & \rightarrow & \diamond^{m+1}, \\ \varphi & \mapsto & [w|_{E_0}, \dots, w|_{E_m}]. \end{cases}$$

If w is sufficiently smooth then it solves the boundary value problem

$$\begin{aligned} \Delta w &= 0 & \text{in } B \setminus \overline{\Omega}, & \quad \frac{\partial w}{\partial \nu} = \varphi & \text{on } \Gamma, \\ \int_{E_\ell} \frac{\partial w}{\partial \nu} \, ds &= 0, & \ell = 0, \dots, m, & \quad \frac{\partial w}{\partial \nu} = 0 & \text{on } T \setminus \bigcup E_\ell, \\ w|_{E_\ell} &= \text{const.}, & \ell = 0, \dots, m, & \quad \sum_{\ell=0}^m w|_{E_\ell} = 0. \end{aligned} \quad (8.9)$$

For the adjoint operator

$$L_E^* : \begin{cases} \diamond^{m+1} & \rightarrow & \mathcal{L}_{\diamond}^2(\Gamma), \\ [J_0, \dots, J_m] & \mapsto & \psi, \end{cases}$$

we have to take the trace $\psi = v|_{\Gamma}$ of the solution $v \in H_{\diamond,E}^1(B \setminus \overline{\Omega})$ of the variational problem

$$\int_{B \setminus \overline{\Omega}} \text{grad } v \cdot \text{grad } V \, dx = \sum_{\ell=0}^m J_\ell V|_{E_\ell} \quad \text{for all } V \in H_{\diamond,E}^1(B \setminus \overline{\Omega}).$$

As in [4] it can then be shown that

$$R - R_0 = L_E D_E L_E^* \quad (8.10)$$

for some isomorphism $D_E : H_{\diamond}^{1/2}(\Gamma) \rightarrow H_{\diamond}^{-1/2}(\Gamma)$ which also satisfies the coercivity inequality (3.11).

Essentially the same argument as in Section 3 can be used to show that L_E^* is injective and hence L_E surjective, so that

$$\mathcal{R}(R - R_0) = \mathcal{R}(R - R_0)^{1/2} = \underset{\diamond}{m+1}.$$

Because of the different boundary conditions in (3.5) and (8.9), however, we should not use the modified dipole potential H_z of (2.8) to test for the cavities Ω . Rather, one has to construct a solution of a boundary value problem of the form (8.9) with a dipole-type singularity at a prescribed point $z \in B$.

We achieve this in the following way. We start with the standard Green's function for the unit disk with singularity in z ,

$$G_z(x) = \begin{cases} -\frac{1}{2\pi} \left(\log|x-z| - \log \left| \frac{z}{|z|} - |z|x \right| \right), & z \neq 0, \\ -\frac{1}{2\pi} \log|x|, & z = 0, \end{cases}$$

and take the directional derivative with respect to z in direction $d \in \mathbb{R}^2$, $|d| = 1$, to obtain a harmonic function from $H_{\diamond, E}^1(B \setminus \overline{\Omega})$ with a dipole-type singularity. With slight abuse of notation we call this function D_z again, i.e.

$$D_z(x) = d \cdot \text{grad}_z G_z(x) = \begin{cases} -\frac{1}{2\pi} \left(\frac{(z-x) \cdot d}{|z-x|^2} - \frac{(|x|^2 z - x) \cdot d}{|z/|z| - |z|x|^2} \right), & z \neq 0, \\ -\frac{x \cdot d}{2\pi} \left(1 - \frac{1}{|x|^2} \right), & z = 0. \end{cases}$$

In a second step, we augment D_z by the (in B) harmonic function $v_z \in H^1(B) \cap H_{\diamond, E}^1(B \setminus \overline{\Omega})$ which satisfies

$$\int_{E_\ell} \frac{\partial v_z}{\partial \nu} ds = - \int_{E_\ell} \frac{\partial D_z}{\partial \nu} ds, \quad \ell = 0, \dots, m, \quad \frac{\partial v_z}{\partial \nu} = - \frac{\partial D_z}{\partial \nu} \quad \text{on } T \setminus \bigcup E_\ell.$$

For $z \in \Omega$ the sum $D_z + v_z$ has all desired features and solves the boundary value problem (8.9) with $\varphi = \frac{\partial}{\partial \nu}(D_z + v_z)$ on Γ .

While we restrict our attention here to the shunt model we would like to remark that it is possible to extend the analysis to a more elaborate model (called 'complete model' in [33]) which also takes contact impedances at the electrodes into account.

The following numerical results correspond to real data measured by the RPI system [30]. The picture in Figure 14 shows the experimental setup for a first example. It contains one cylindrical piece of metal in a homogeneous saline-filled tank. The metal is, of course, not insulating; in fact, it behaves as an inclusion with a higher conductivity than the background, but this does not affect our method (see [4]). The eigenvalues of $R_0 - R$ are also shown in Figure 14. In view of the experiments of the previous sections we are led to use only $m_0 = 2$ (averaged) eigenvalues for the reconstruction. Still, pretty good results are achieved by the factorization method as well as the MUSIC algorithm, see Figure 15.

In our second example shown in Figure 16 there are two metal pieces and one piece of plastic in the tank. This time, up to four eigenvalues can be used to compute reconstructions. Recall, however, that even with four eigenvalues it has not been possible to reconstruct the three cavity phantom with the factorization method, see Section 5. As can be seen in the left-hand plot of Figure 17 the same is true here. Not so for the MUSIC reconstruction shown in the middle plot of Figure 17: Like for the simulated data in Section 6 (cf. Figure 7) this reconstruction is reasonable.

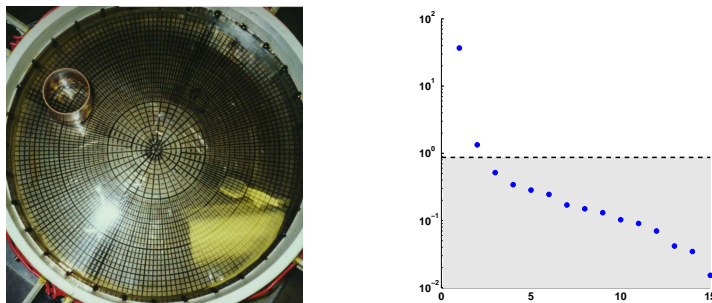


Figure 14. Experiment 1: Setup and eigenvalues of $R_0 - R$.

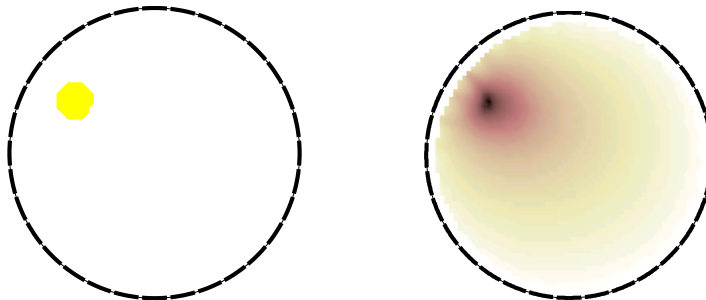


Figure 15. Experiment 1: Reconstructions with $m_0 = 2$.

The third plot in this figure is the power visualization of the factorization method (as in Figure 10). This reconstruction is again similar to the MUSIC one and seems to provide a useful alternative for very noisy data.

We should mention that we have also tested the complete electrode model for these data but the results were about the same whatever value we assigned to the contact impedance. We believe that other modelling errors are much more important here. In fact, as shown in [33], for each of the electrode models, R_0 can be diagonalized by the discrete Fourier vectors. However, measuring the Frobenius norm of the resulting off-diagonal entries we found them to dominate the measurement noise by a factor of over 40. Possibly this additional error is caused by the 2D approximation of a 3D reality, but this needs further investigation.

9. Concluding remarks

We shall close with a brief account of related work and possible extensions of the above results. To begin with, we emphasize that the factorization method originated in inverse scattering theory with a fundamental paper by Andreas Kirsch [22]. In this paper, Kirsch put earlier investigations by Colton and himself [12] (the so-called linear sampling method, see also the survey by Colton, Coyle and Monk [11]) in a proper context, and developed what is now called the factorization method in inverse scattering.

Subsequently, a similar theory was developed for electrical impedance tomography, independently in [4] and by Hähner in [19]; see also Kress and Kühn [26]. By restricting ourselves to insulating cavities in this survey, we only touched upon the

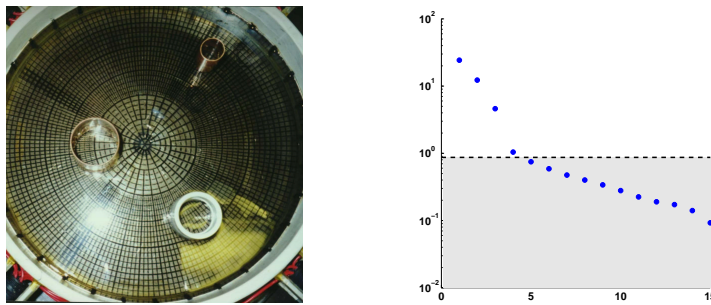


Figure 16. Experiment 2: Setup and eigenvalues.

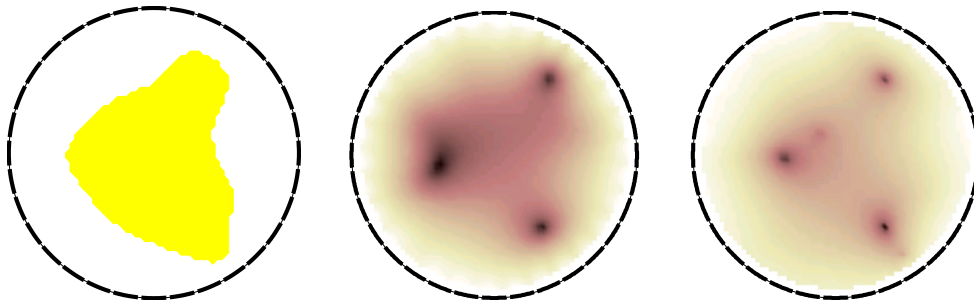


Figure 17. Experiment 2: Reconstructions with $m_0 = 4$.

full generality of this theory, compare [4].

We also mention that the factorization method can be extended to find cracks within two dimensional domains, see Kirsch and Ritter [24] for the inverse scattering problem, and [7] for the electrical impedance case.

Currently, we work on the adaption of our codes to realistic data acquisition models and to 3D reconstructions. In these cases the major difficulty is the efficient computation of the test functions h_z (see Subsection 4.1).

Appendix: The range of $\Lambda - \Lambda_0$

In this appendix we comment on the difference between the preliminary algorithm from the end of section 2 and the factorization method by proving a characterization of $\mathcal{R}(\Lambda - \Lambda_0)$ analogous to (3.14) under a certain restriction of the generality of the setting. We consider a bounded and simply connected domain B in \mathbb{R}^n , $n \geq 2$, and a simply connected subdomain Ω (one insulating cavity) with $\overline{\Omega} \subset B$. In addition we assume that the Schwarz reflection principle (cf, e.g., [18]) allows to reflect the *entire* domain $B \setminus \overline{\Omega}$ into the cavity Ω . We denote this reflected domain by B' (see figure A1).

Theorem 1. *Let $h_z = H_z|_T$ with H_z defined as in (2.8), and the above assumptions be satisfied. Then there holds*

$$h_z \in \mathcal{R}(\Lambda - \Lambda_0) \quad \text{if and only if} \quad z \in \Omega \setminus \overline{B'}.$$

Proof. For a proof we first recall that $h_z \in \mathcal{R}(\Lambda - \Lambda_0)$ implies $h_z \in \mathcal{R}(\Lambda - \Lambda_0)^{1/2}$ and, by virtue of (3.14), we can therefore restrict our attention to points $z \in \Omega$.

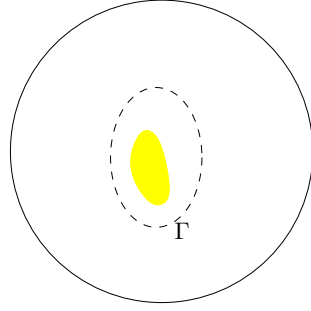


Figure A1. Sketch of the geometry in theorem 1. The yellow shaded region shows $\Omega \setminus \overline{B'}$.

So, let $z \in \Omega \setminus \overline{B'}$ be arbitrarily chosen and note that H_z is the distributional solution of the Neumann boundary value problem

$$\Delta H_z = d \cdot \text{grad}_z \delta(\cdot - z) \quad \text{in } B, \quad \frac{\partial}{\partial \nu} H_z = 0 \quad \text{on } T.$$

Accordingly, let H'_z be the distributional solution of the same differential equation in Ω with boundary values on $\Gamma = \partial\Omega$, i.e.

$$\Delta H'_z = d \cdot \text{grad}_z \delta(\cdot - z) \quad \text{in } \Omega, \quad \frac{\partial}{\partial \nu} H'_z = 0 \quad \text{on } \Gamma.$$

By reflection, H'_z can be extended to a harmonic function in $B \setminus \{z\}$, again denoted by H'_z , with flux $\psi = \partial H'_z / \partial \nu$ on the outer boundary T . This function provides the solution of the boundary value problem (2.1), (2.2) for $f = \psi$. By construction, the difference $H'_z - H_z$ is harmonic in all of B and its Neumann boundary values on T are the same as those of H'_z . This shows that $u_0 = H'_z - H_z$ is the solution of the boundary value problem (2.3) for $f = \psi$ and hence

$$(\Lambda - \Lambda_0)\psi = H'_z|_T - (H'_z - H_z)|_T = H_z|_T = h_z,$$

as required.

Vice versa, assume that $h_z \in \mathcal{R}(\Lambda - \Lambda_0)$, i.e. $h_z = (\Lambda - \Lambda_0)f$ for some $f \in \mathcal{L}^2_\infty(T)$. Furthermore, denote by u and u_0 the solutions of the boundary value problems (2.1), (2.2), and (2.3), respectively. Since u has vanishing flux on Γ it can be extended by reflection to a harmonic function on $(B \setminus \overline{\Omega}) \cup B' \cup \Gamma$. By the uniqueness of the Cauchy problem (3.13) $u - u_0$ therefore coincides with H_z on $(B \setminus \overline{\Omega}) \cup B' \cup \Gamma$ and, as in section 3, this implies that $z \notin \overline{B'}$. \square

We finally mention that for the case where B is the unit disk and Ω a concentric disk with radius $\varrho < 1$ it is shown in [4] that $h_z \in \mathcal{R}(\Lambda - \Lambda_0)$ if and only if $|z| < \varrho^2$. This coincides with the set $\Omega \setminus \overline{B'}$, where B' is obtained by reflection of the annulus at the circle $|x| = \varrho$. Here the reflection is given by $x \mapsto \varrho^2 x / |x|^2$.

Acknowledgments

We like to thank Birgit Schappel for providing us with Figure 2. The data sets from Section 8.2 have been taken while the second author was visiting RPI. He gratefully acknowledges the hospitality and support of Margaret Cheney, David Isaacson, and Jon Newell that he received.

References

- [1] Alessandrini G 1988 Stable determination of conductivity by boundary measurements *Appl. Anal.* **27** 153–72
- [2] Barceló B, Fabes E and Seo J K 1994 The inverse conductivity problem with one measurement: uniqueness for convex polyhedra *Proc. Amer. Math. Soc.* **122** 183–9
- [3] Borcea L 2002 Electrical impedance tomography *Inverse Problems* **18** R99–R136
- [4] Brühl M 2001 Explicit characterization of inclusions in electrical impedance tomography *SIAM J. Math. Anal.* **32** 1327–41
- [5] Brühl M, Gebauer B and Hanke M 2002 GEIT: a graphical user interface for electrical impedance tomography <http://numerik.mathematik.uni-mainz.de/geit>
- [6] Brühl M and Hanke M 2000 Numerical implementation of two noniterative methods for locating inclusions by impedance tomography *Inverse Problems* **16** 1029–42
- [7] Brühl M, Hanke M and Pidcock M 2001 Crack detection using electrostatic measurements *M2AN Math. Model. Numer. Anal.* **35** 595–605
- [8] Brühl M, Hanke M and Vogelius M S 2003 A direct impedance tomography algorithm for locating small inhomogeneities *Numer. Math.* **93** 635–54
- [9] Cheney M 2001 The linear sampling method and the MUSIC algorithm *Inverse Problems* **17** 591–6
- [10] Cheney M, Isaacson D and Newell J C 1999 Electrical impedance tomography *SIAM Rev.* **41** 85–101
- [11] Colton D, Coyle J and Monk P 2000 Recent developments in inverse acoustic scattering theory *SIAM Rev.* **42** 369–414
- [12] Colton D and Kirsch A 1996 A simple method for solving inverse scattering problems in the resonance region *Inverse Problems* **12** 383–93
- [13] Dautray R and Lions J-L 1990 *Mathematical Analysis and Numerical Methods for Science and Technology* (Berlin: Springer)
- [14] Devaney A J Super-resolution processing of multi-static data using time reversal and MUSIC *J. Acoust. Soc. Amer.* to appear
- [15] Di Cristo M and Rondi L 2003 Examples of exponential instability for inverse inclusion and scattering problems *Inverse Problems* **19** 685–701
- [16] Friedman A and Isakov V 1989 On the uniqueness in the inverse conductivity problem with one measurement *Indiana Univ. Math.* **38** 563–79
- [17] Friedman A and Vogelius M S 1989 Identification of small inhomogeneities of extreme conductivity by boundary measurements: a theorem on continuous dependence *Arch. Ration. Mech. Anal.* **105** 299–326
- [18] Garabedian P R 1964 *Partial Differential Equations* (New York: Wiley)
- [19] Hähner P 1999 An inverse problem in electrostatics *Inverse Problems* **15** 961–75
- [20] Henrici P 1986 *Applied and Computational Complex Analysis* Vol 3 (New York: Wiley)
- [21] Isakov V 1988 On uniqueness of recovery of a discontinuous conductivity coefficient *Comm. Pure Appl. Math.* **41** 865–77
- [22] Kirsch A 1998 Characterization of the shape of the scattering obstacle using the spectral data of the far field operator *Inverse Problems* **14** 1489–512
- [23] Kirsch A 2002 The MUSIC algorithm and the factorization method in inverse scattering theory for inhomogeneous media *Inverse Problems* **18** 1025–40
- [24] Kirsch A and Ritter S 2000 A linear sampling method for inverse scattering from an open arc *Inverse Problems* **16** 89–105
- [25] Kohn R V and Vogelius M S 1985 Determining conductivity by boundary measurements II. Interior results *Comm. Pure Appl. Math.* **38** 643–67
- [26] Kress R and Kühn L 2002 Linear sampling methods for inverse boundary value problems in potential theory *Appl. Numer. Math.* **43** 161–73
- [27] Mandache N 2001 Exponential instability in an inverse problem for the Schrödinger equation *Inverse Problems* **17** 1435–44
- [28] Nachman A I 1988 Reconstructions from boundary measurements *Ann. of Math.* **125** 531–76
- [29] Nachman A I 1995 Global uniqueness for a two-dimensional inverse boundary value problem *Ann. of Math.* **142** 71–96
- [30] Newell J C 2000 <http://www.rpi.edu/~newelj/eit.html>
- [31] Schappel B Electrical impedance tomography in the half space: locating obstacles by electrostatic measurements on the boundary *Proc. 3rd World Congress on Industrial Process Tomography* to appear
- [32] Seo J K 1996 On the uniqueness in the inverse conductivity problem *J. Fourier Anal. Appl.* **2**

227–35

- [33] Somersalo E, Isaacson D and Cheney M 1992 Existence and uniqueness for electrode models for electric current computed tomography *SIAM J. Appl. Math* **52** 1023–40
- [34] Stewart G W 2001 *Matrix Algorithms* Vol II (Philadelphia: SIAM)